Journal of Nuclear Materials 403 (2010) 89–100

Contents lists available at ScienceDirect

Journal of Nuclear Materials

journal homepage: www.elsevier.com/locate/jnucmat

Microstructure evolution of irradiated tungsten: Crystal effects in He and H implantation as modelled in the Binary Collision Approximation

M. Hou [a,*], C.J. Ortiz [b], C.S. Becquart [c], C. Domain [d], U. Sarkar [e], A. Debacker [c]

[a] Physique des Solides Irradiés et des Nanostructures CP234, Université Libre de Bruxelles, Bd du Triomphe, B-1050 Brussels, Belgium
[b] Laboratorio Nacional de Fusión por Confinamiento Magnético, CIEMAT, E-28040 Madrid, Spain
[c] Unité Matériaux Et Transformations (UMET), UMR 8207, Université de Lille 1, F-59655 Villeneuve d'Ascq Cedex, France
[d] EDF-R&D Département MMC, Les Renardières, F-77818 Moret sur Loing Cedex, France
[e] Physics Department, Assam University, Silchar, India

ARTICLE INFO

Article history:
Received 5 March 2010
Accepted 1 June 2010

ABSTRACT

It is important to develop an understanding of the evolution of W microstructure the conditions the International Thermonuclear Experimental Reactor (ITER) as well as the DEMOnstration Power Plan (DEMO), and modelling techniques can be very helpful. In this paper, the Binary Collision Approximation of Molecular Dynamics as implemented in the Marlowe code is used to model the slowing down of atomic helium and hydrogen on tungsten in the 1–100 keV range. The computed helium and Frenkel Pairs (FP) distributions are then used as input for the simulation of isochronal annealing experiments with an Object Kinetic Monte Carlo (OKMC) model. Parameterisation is discussed in a companion paper to this one.

To model inelastic energy losses beyond the Lindhard regime, a new module has been implemented in the Marlowe code which is presented here, along with a discussion on various parameters of the model important in the modelling of channelled trajectories. For a given total inelastic stopping cross section, large differences in low energy channelling ranges are identified depending on whether inelastic energy loss is considered to be purely continuous or to also occur during the atomic collisions. In polycrystals, the channelling probability is shown to be significant over the whole range of slowing down energies considered. Channelling together with short replacement sequences has the effect of reducing the FP production efficiency by more than a factor two in polycrystalline as compared with an hypothetical structureless tungsten. This has a crucial effect on the helium isochronal desorption spectra predicted by the OKMC simulations. Those predicted with structureless tungsten are at variance with experiment, due to the overestimation of He trapping on the radiation induced defects.

1. Introduction

One of the main issues of nuclear fusion technology is the interaction between the excited plasma and the wall in which it is confined. This wall is irradiated by an intense current of various species produced by fusion reactions. These species are essentially light ions and 14 MeV neutrons. The consequences are the backscattering of a fraction of the ions, neutralised at the wall surface and the sputtering of surface atoms, also mainly in a neutral state, that reduce the quality of the plasma. At the same time, partial redeposition together with radiation-induced surface segregation modify the surface chemical composition and thereby the plasma–wall interaction properties. These effects are particularly crucial in specific areas of the wall, such as the divertor in tokamaks subjected to particularly intense irradiation. Another major consequence of this high dose and high flux irradiation is the degradation in the long term of the mechanical properties of the wall material, because of damage generated by the implanted ions and neutrons.

This paper focuses on hydrogen and helium penetration as well as related atomic displacement, while a companion paper discusses the parameterisation for fusion conditions of an Object Kinetic Monte Carlo (OKMC) code to predict the microstructural evolution of irradiated tungsten up to the mesoscopic scale [1]. These are part of a broad effort to set up predictive models of reactor materials under irradiation covering the range of scales from the atomic level to macroscopic [2–7]. More specifically, the purpose of the present paper is to provide this information using the Binary Collision Approximation to classical molecular dynamics, taking into account the polycrystalline nature of wall materials as realistically as possible. As will be shown in the last sections, the anisotropic nature of polycrystals at the atomic scale has a marked impact on mesoscopic model predictions.

* Corresponding author. Tel.: +32 2 6505735; fax: +32 2 6505227.
E-mail address: mhou@ulb.ac.be (M. Hou).

0022-3115/$ - see front matter © 2010 Elsevier B.V. All rights reserved.
doi:10.1016/j.jnucmat.2010.06.004

The BCA is well-established in the sense that a large amount of results illustrates its capabilities and limitations. We found it useful however to re-visit some of them in the light of the slowing down conditions relevant to plasma–wall interaction. The focus will be on modelling penetration and the related short term phenomena at the origin of long term evolution. The important area of surface effects will be left aside as their complexity is not yet accounted for in the presently available mesoscopic models. In particular, we shall study the slowing down of H and He ions on tungsten. H and He represent the lightest and the heaviest atoms slowing down from the plasma onto the wall at high flux and dose. On the other hand, W was selected since, thanks to its efficient thermal and mechanical properties, it represents a privileged candidate for the divertor material in ITER. All the BCA trajectories presented in this work are simulated with the version 15 of the Marlowe code [8]. In Section 2, we start by discussing the magnitude of directional effects on the light ion trajectories, on the basis of the string model of channelling [9]. Next, some details of the BCA parameterisation for crystalline systems is examined, which is relevant to the case of light ion trajectories and a new module for the Marlowe code is presented to model energy loss to electronic excitation in the multiple collision and in the Bethe regimes. The consequences of the inelastic energy loss model on H and He range profiles as well as of the target model and the BCA parameters are discussed. Section 3 is devoted to the parameterisation of the displacement cascade model. In our previous work about the modelling of displacement cascades in iron, this parameterisation was made on the basis of full MD calculations [10]. To our knowledge, only limited MD data is available for W [11]. On the other hand, direct observation data by Field Ion Microscopy of displacement cascades in W with atomic resolution are available, as generated by a number of different heavy ions [12,13] and these are used, with the same approach as with MD cascades in [10]. Damage distributions are then computed and compared with H and He penetration ranges with slowing down energies between 1 keV and 100 keV.

Section 4 is devoted to the OKMC modelling of post-irradiation ageing experiments on the basis of BCA predictions regarding He penetration and induced atomic displacements. The crystalline effects in W polycrystals are emphasised.

2. The BCA of the He–W and H–W interactions

The range of ion energies relevant to plasma–wall interactions spans over more than six orders of magnitude from eV to more than 10 MeV as transmutation products are concerned. In the eV regime, little He or H penetrates the surface and, when it does, the penetration depth is so shallow that, unless pre-existing trapping centres are present, it is spontaneously driven to the surface by the elastic stress field and desorbs. Hence, in this regime, the helium-surface interaction is mainly governed by adsorption, desorption and eventually backscattering.

In the 10–100 eV range, thermal helium desorption spectroscopy evidences the penetration of helium and even some damage production, although the damage production efficiency was found to be one to two orders of magnitude smaller than predicted with the Kinchin and Pease model [14,15]. In this regime, spontaneous recombination of close vacancy–interstitial pairs, which are not accounted for by the Kinchin and Pease model, plays an important role in limiting the Frenkel pair formation. In addition, a few tens of eV are sufficient for the trajectories and subsequent atomic displacements to be influenced by the crystal lattice effects such as channelling and focusing chains. In higher energy atomic collisions, energy loss partitions between elastic and inelastic via nuclear encounters and electron excitations, respectively. The nuclear scattering cross-section passes a maximum, vanishes at the limit of high energy, while the inelastic scattering cross section linearly increases with velocity, levels off in the so-called multiple collision regime when the velocity of the ion compares with that of orbital electrons, in a range where the nuclear stopping is already negligible, and finally decreases with energy at still higher velocity, in the Bethe regime [16].

Hence, in order to model properly the ballistic interaction of hydrogen and helium with crystalline or polycrystalline matter, as tungsten typically is, three aspects need to be carefully considered, namely, crystal lattice effects, energy loss mechanisms, and vacancy–interstitial recombinations. The latter is no part of the BCA and will be discussed separately.

The BCA consists in computing the development of cascade trajectories triggered by an energetic atom as a sequence of binary collisions rather than integrating the equations of motion of the whole system over time. Such an approximation is reasonable when a limited number of atoms move in an area where the other atoms may be considered at rest, without significant interaction between them. In the Marlowe code employed here, binary collisions are characterised by an impact parameter and the scattering integrals [17]. Since energy transfers that are too low to generate atomic displacements are not relevant to damage production, collisions with an impact parameter larger than a preset value are neglected and a maximum impact parameter is assumed. Energy may be lost elastically (nuclear encounters) and inelastically (electronic excitations) and binary collisions are described in the quasi-elastic approximation. Elastic losses result from atomic interactions governed by a binary interaction potential, usually chosen as purely repulsive. In the present simulations, the screened Coulomb function in [18] is used. Potential target atoms are selected within a cell containing a limited number of atoms within the appropriate crystallographic structure, translated in the vicinity of the projectile. To model a polycrystal, the structure is rotated at random before each projectile is initiated and its orientation is kept constant until the cascade calculation is terminated, before the next projectile is initiated. In this way, it is assumed that the spatial extent of the cascade is smaller than the grain size. An amorphous medium may also be modelled by letting the crystal structure undergo a random rotation before each collision. This way, directional correlations are destroyed while the first neighbour distances are preserved. A scattered atom is assumed to be set into motion if its kinetic energy at the exit of the collision is larger than a preset value. One also accounts for its binding energy to a lattice site. Thermal disorder may be accounted for, and in this work, small random thermal displacements of W atoms from their lattice sites are considered with a mean squared root amplitude of 0.125 Å. According to the Debye–Waller model [19], this corresponds to a temperature of 300 K.

In the next sections, we discuss the consequence of channelling (Section 2.1) and inelastic energy loss (Section 2.2) on penetration ranges. The question of recombination in cascades is addressed in Section 3.2.

2.1. Directional effects

2.1.1. Channelling probability

The main underlying assumption to range calculations, the linearised Boltzmann transport [20–22] and popular Monte Carlo simulations codes [23], is that of a structureless medium. However, typical grain sizes in polycrystalline solids are of the order of the micron, which is still one order of magnitude larger than the range of 100 keV He atoms slowed down under channelling conditions in tungsten. BCA simulations indicate that this also holds for H atoms in the same energy range. Hence, in polycrystals, the largest part of the trajectory is subjected to the influence of the crystal lattice. In a

crystal grain, energetic light particle beams partition into a channelled fraction, governed by correlated scattering in low index crystallographic directions and a "random" fraction, the motion of which is insensitive to lattice directional correlations. In Lindhard's model [9], channelling occurs when the angle of incidence is lower than a critical value such that the atomic rows may be assimilated to continuous strings. The conditions for the channelling of an atom with energy E was given by Lindhard as

$$\Psi_1 = \sqrt{\frac{E_1}{E}} \quad \text{for } E > E' \tag{1a}$$

$$\Psi_2 = \sqrt{\frac{a}{d_{hkl}}\Psi_1} \quad \text{for } E < E' \tag{1b}$$

with

$$E' = 2Z_1 Z_2 e^2 \frac{d_{hkl}}{a^2} \tag{1c}$$

and

$$E_1 = \frac{2Z_1 Z_2 e^2}{d_{hkl}} \tag{1d}$$

where $\psi_{1,2}$ is the critical angle for channelling in a crystallographic direction with atomic spacing d_{hkl}. Z_1 and Z_2 are the atomic charge of the projectile and the target atoms and a is a screening distance. In the case of the slowing down of He in W, using the screening distance of the potential $a = 0.88543 a_B (Z_1^{2/3} + Z_2^{2/3})^{-1} = 0.12125$ Å [18], where a_B is the Bohr radius, according to [24], we get E' 007E 795 keV for He ⟨1 1 1⟩ channelling. For H, the screening distance is $a = 0.127$ Å, we get $E' \sim 362$ keV, also for ⟨1 1 1⟩ channelling. In the present study, only energies lower than 100 keV are considered. The critical angle ψ_2 is represented as a function of He energy for ⟨1 0 0⟩, ⟨1 1 0⟩ and ⟨1 1 1⟩ directions in tungsten in Fig. 1. Assuming that the polycrystal grains are oriented at random with respect to the slowing down direction, it is possible to estimate the channelled fraction of the incident beam from the solid angle subtended by the critical angle in Eq. (1). This fraction is represented in Fig. 1b as a function of the energy of incidence of both He and H in W. Again, only channelling by ⟨1 0 0⟩, ⟨1 1 0⟩ and ⟨1 1 1⟩ directions is considered, whereas channelling by higher index directions as well as planar channelling is neglected. Fig. 1 indicates that channelling conditions are always encountered when the He (H) energy is less than 3 (2) keV. It remains above 30% at 10 (6) keV and falls down to 6 (3)% at 60 keV and 4 (2)% at 100 keV.

It should be noted that Eq. (1) may be regarded leads to a lower limit of the channelling probability. Indeed, at larger angles than Ψ_2 and at low energy, when the momentum approximation breaks down, the critical angle may increase [25] and enhanced penetration is thus still possible. Furthermore, the orientation of grains with respect to surfaces are not fully at random as low index crystallographic surfaces have low excess energies and are therefore thermodynamically favored.

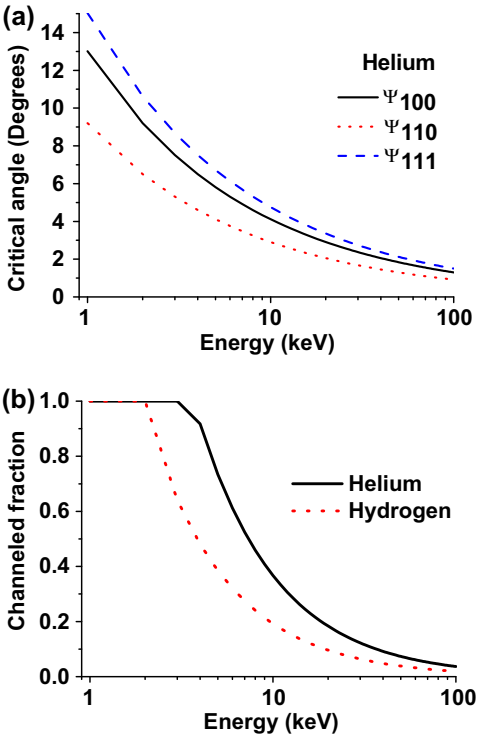

Fig. 1. The energy dependence (a) of the He critical channelling angle on ⟨1 0 0⟩, ⟨1 1 0⟩ and ⟨1 1 1⟩ directions in tungsten and (b) of the H and He channelled fraction in case of slowing down on the surface of polycrystalline tungsten.

2.1.2. Simultaneous collisions

The modelling of channelled trajectories in the BCA raises an issue as the flux is peaking in the centre of the channels. Indeed, in such conditions, the projectiles cross symmetrical rings of atoms with which they undergo simultaneous collisions with comparable impact parameters. Assuming simultaneous collisions to occur independently leads to an overestimate of the elastic energy loss and an underestimate of the focusing into the channels. The BCA thus breaks down and an approximate treatment is necessary. The strategy adopted in the Marlowe code [8,30] is to compute the scattering integrals of each projectile–target atoms pair independently between simultaneous collision partners with the constraint of momentum conservation. Scattered kinetic energies are then scaled in order to warrant energy conservation. This strategy proved to be reasonable in a number of cases [30,31]. A criterion is then necessary for deciding whether collisions with potential partners are simultaneous or not. This criterion is depicted in Fig. 2. In order for simultaneous collisions to occur, two conditions must be met: (i) the projection of the potential target positions on the projectile momentum both must lay within the overlap of spheres centred on the target atoms having a radius equal to the maximum impact parameter, b_{max}; (ii) the distance between these projections, corresponding to ξ in Fig. 2, needs to be smaller than a preset value, ξ_{lim}. Hence, the channelling efficiency is governed by two parameters, one is the maximal impact parameter in a binary collision and the second is the parameter ξ_{lim}. Since channelling also

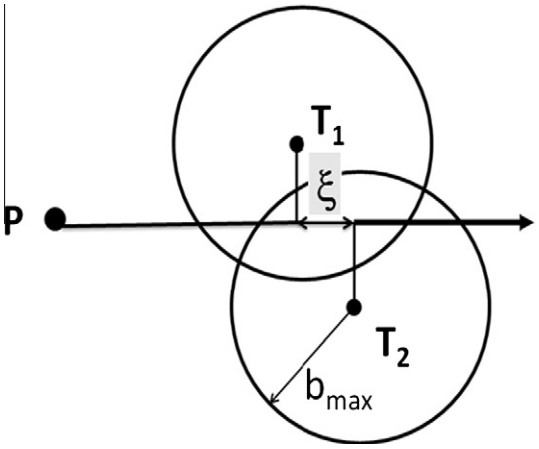

Fig. 2. Scheme used as a criterion for treating the collision of projectile P with the potential target atoms T_1 and T_2 as simultaneous. The arrow indicates the direction of the momentum of the incident projectile. The definition of parameters b_{max} and ξ is given in the text.

depends on the projectile energy, as discussed in Section 2.1, its efficiency also depends on the model for inelastic energy loss. The consequences of these collision parameters on implantation profiles are discussed in Section 3.2.

2.2. Energy loss

As mentioned above, along an energetic ion trajectory, energy is transferred to both the nuclear and the electronic systems. In what follows, nuclear encounters are regarded as governed by a central repulsive potential. The one used in what follows is the screened Coulomb potential with the screening function in Ref. [18].

2.2.1. The Lindhard and the Oen–Robinson models

Several models are available for quantifying the energy lost to electronic excitation. In the Lindhard, Scharff and Schiøtt (LSS) theory [16], the electronic system of the material is regarded as a continuum and has the consequence that the energy loss cross section is proportional to the ion velocity, just as depicted by Ohm's law. This model proved to work remarkably well in a broad range of conditions and may expectedly apply in conditions where electron localisation effects on ion trajectories are small. They are not when the ion velocity is comparable or higher than the Bohr velocity, which corresponds to 25 keV per amu, that is, 100 keV in the case of helium and, obviously, 25 keV for hydrogen.

At lower energies, electronic localisation also plays an important role in the case of collisions between two heavy atoms, when the electric fields associated with the overlapping electronic clouds contribute to the nuclear scattering. In the case of helium and protons, it is not quite clear to which extent the localisation of the electronic density around the nuclei influences their trajectories. A model to account for local effects was designed by Oen and Robinson who suggested that, in the quasi-elastic approximation, the localisation of the inelastic energy losses at the scattering sites had an important effect on helium backscattering from heavy materials [26].

In this model, denoted "OR" in what follows, the magnitude of the energy lost to electrons in a binary collision is related to the distance of closest approach according to:

$$Q(b,E) = \frac{0.045 \cdot K \cdot E^{1/2}}{\pi \cdot a_{12}} \cdot \exp\left(-\frac{0.3 \cdot R(b,E)}{a_{12}}\right) \tag{2}$$

where the distance of closest approach R depends on the impact parameter b and on the projectile energy E. K is a constant which determines the magnitude of Q. In this expression, the form of the exponential is chosen so as to approximate the close distance electronic density of a Thomas-Fermi distribution [27] where a_{12} is the screening length. The electronic stopping power can be derived from Eq. (2) and, in the momentum approximation (according to which $R(b,E) \sim b$), it is shown in [26] to take the form

$$S_e = K \cdot E^{1/2} \cdot (1-\alpha) \tag{3}$$

where typically, $\alpha \ll 1$. In this expression, K is selected in such a way that the energy loss given by Eq. (2) leads to a stopping power close to Lindhard's.

As it is apparent in Eq. (2), the Born–Oppenheimer approximation is used. The scattering integrals are subsequently computed in the quasi-elastic approximation where the energy lost to electron excitation is assumed to occur instantaneously at the apsis of the collisions. This affects the scattering asymptote directions in the system of the laboratory.

In order to account for both local and non-local energy loss due to electron excitation in the calculation of atomic trajectories, we use a weighted average between Eq. (2) and velocity dependent loss according to Lindhard. Since the relative contributions of localised and delocalised electrons to the energy loss are not well-known and hardly estimated experimentally, assuming equipartition is a common practice. The sensitivity of ion penetration ranges and damage profiles on the inelastic loss model is discussed in the next sections.

2.2.2. The Ziegler semi-empirical approach

With further increasing velocities, the transition from the Linhard to the Bethe regime governed by Rutherford scattering is met, which is not accounted for in Marlowe code. Therefore, a specific module that accounts for the whole range of velocities and masses was implemented in Marlowe code. The physical understanding of the transition from the Linhard to the Bethe regime gave rise to an extensive literature which is rationalised in [28]. As is done in a semi-empirical way by Ziegler [18], we used the so-called heavy ion scaling rule to calculate the stopping power of atoms with energies above 25 keV per amu. This semi-empirical rule states that the stopping power of a heavy ion is proportional to the hydrogen stopping power and can be simply expressed as:

$$S_{HI} = S_H \cdot (Z^*_{HI})^2 = S_H \cdot Z^2_{HI} \cdot \gamma^2 \tag{4}$$

where S_{HI} is the stopping power of the heavy ion, Z_{HI} its atomic number, Z^*_{HI} its effective charge and γ its fractional effective charge. The latter continually changes depending on the ion velocity and the electronic density of the target. In addition, the ion charge density also polarizes and changes its shape due to the polarization of target electrons in front and around the ion. Hence, according to Eq. (4), if the stopping power of hydrogen is known, it is only necessary to calculate the fractional effective charge of the incident ion to obtain its stopping power. In this work, the stopping power of hydrogen—S_H in Eq. (4)—was taken from SRIM 2003 code [23]. In the following we shall consider energy loss of medium velocity ions and briefly summarize how the fractional effective charge of heavy ions can be calculated in the framework of the Brandt and Kitagawa theory (BK) [29], which has shown to adequately describe the loss of heavy ions between the Linhard and the Bethe regimes.

The first major concern is to calculate the stripping of the ion by comparing the ion velocity to the velocity of the target electrons. As can be shown (see Eqs. (3-22)–(3-38) from Ref. [18]), the fractional effective charge of a heavy ion at medium velocity in a solid can be expressed as follows:

$$\gamma = q + (1-q) \cdot \frac{(V_B/V_F)^2}{2} \cdot \ln\left[1 + \left(\frac{2 \cdot \Lambda \cdot V_F}{a_B \cdot V_B}\right)^2\right] \tag{5}$$

where V_B is the Bohr velocity, V_F is the Fermi velocity of target electrons, a_B the Bohr radius, Λ the screening length that characterises the electron density distribution of the ion, and q the degree of ionisation of the ion. Note that the fractional ionisation q is different from the ion's effective charge γ. A detailed expression of Λ is given by Eq. (3-31) of Ref. [18]. The first term of Eq. (5), q, corresponds to distant collisions, i.e. for target electrons that do not penetrate the ion's electronic volume. The second term of Eq. (5) corresponds to the increase of energy loss due to some target electrons that penetrate the ion's electronic cloud. The final consideration to evaluate the electronic stopping power of the heavy ions is to calculate the degree of ionisation q. Following the extension of the BK theory found in Ref. [18], the ionisation level of the ion can be expressed as:

$$q = 1 - \exp\left[-c \cdot \left(\frac{V_{rel}}{V_B \cdot Z^{2/3}_{HI}} - d\right)\right] \tag{6}$$

where c and d are constants and V_{rel} is the relative velocity between the incident ion and the target electrons. Constants c and d where obtained by fitting a large set of experimental stopping powers, as shown in Ref. [18]; the best agreement was obtained for $c = 0.95$ and $d = 0.07$.

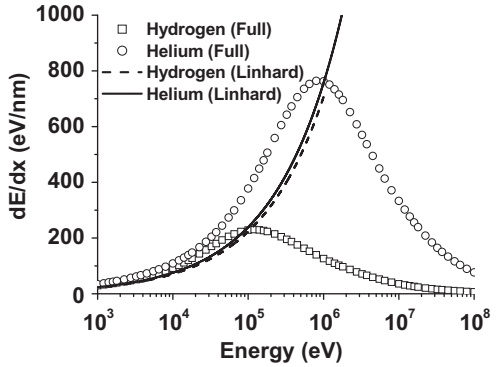

Fig. 3. Semi-empirical estimate of the energy dependence of the stopping cross section of He and H in tungsten, according to Ref. [23].

The electronic stopping cross section as a function of energy for H and He is presented in Fig. 3 which shows that in the 10 keV range, the H and He cross sections are similar. Their difference becomes substantial in the 100 keV range and above, when the H stopping cross-section passes a maximum, which is also the highest slowing down energy considered in this work.

2.2.3. Channels of energy loss helium and hydrogen energy

Using the equipartition rule for He and Ziegler's approach for H, we now consider the different channels of energy loss in W, in the 1–100 keV slowing down energy range.

In the case of He and H irradiation, the energy carried by sputtered atoms represents a very small fraction of the slowing down energy. Indeed, most of the kinetic energy of a sputtered atom is of the order of the cohesive energy of the material (in the eV range) and the sputtering yield of W for He and H is low. The energy of incidence is thus mainly dissipated via three processes, namely, electronic excitations (inelastic energy loss), nuclear encounters (damage energy) and backscattering. Fig. 4 provides their estimates as function of the ion energy in case of normal incidence in various types of W targets. These are either a single crystal with a (1 1 1) surface (similar trends are found with (1 0 0) and (1 1 0) surfaces), a polycrystal or an amorphous target. These results have been obtained with Marlowe using the model depicted above. In the whole range of energy of incidence investigated, more than 90% of the energy is lost to electronic excitation. Next comes the damage energy, which may contribute to permanent atomic displacements. The backscattered energy compares with the damage energy, although systematically lower. In contrast with inelastic loss, damage and backscattered energies are sensitive to the target model. As a consequence of channelling in the single crystal case, the mean H and He backscattering energies pass a maximum in the 5–20 keV range. Beyond, it is a decreasing function of the energy of incidence as the channelling efficiency increases. In such conditions, the energy available for damage levels off and damage production in channelling conditions is not any further an increasing function of the energy.

In what follows, the sensitivity of penetration profiles on the inelastic energy loss model and on other parameters involved in the computation of trajectories is estimated, with particular attention to those affecting focusing into low index channel directions.

3. Implantation and damage profiles

3.1. Implantation

In Fig. 5, penetration depth distributions of 10 keV He are compared in the case of the slowing down on (1 0 0), (1 1 0), (1 1 1), polycrystalline and amorphous surfaces using different inelastic

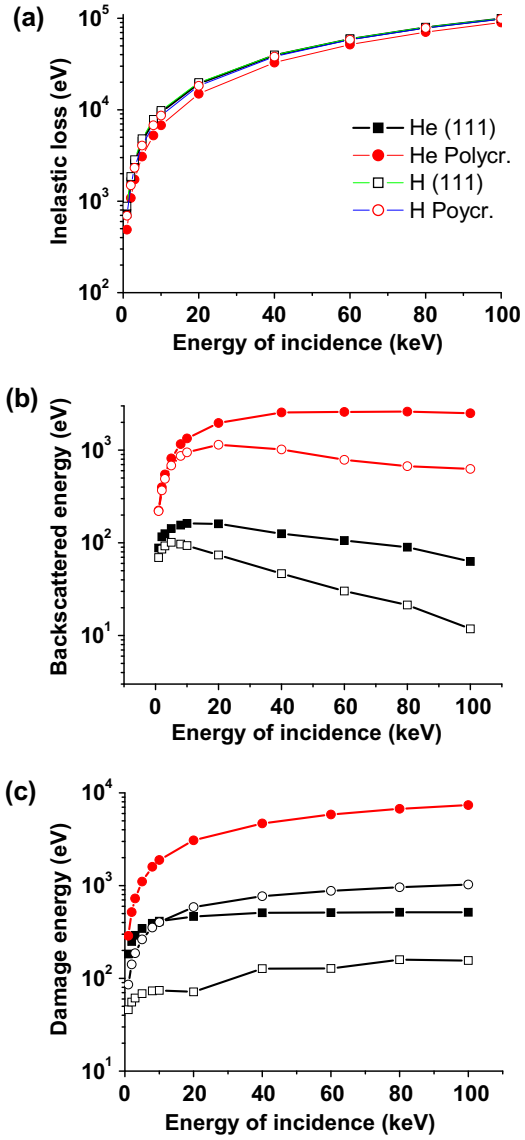

Fig. 4. Dependence on the H and He slowing down energy (a) of the inelastic energy loss, (b) of the energy carried by the backscattered atoms and (c) of the damage energy. The projectiles are normally incident. The cases are compared for a single crystal tungsten target with a (1 1 1) surface (similar trends are found with (1 0 0) and (1 1 0) surfaces) and of polycrystalline tungsten.

loss models, impact parameters and ξ_{lim}-values. The results are displayed when using either the LSS electron loss model only and assuming equipartition between OR and LSS losses. The simulations are also repeated using two different values of the maximum impact parameter in the BCA. One, $b^1_{\mathrm{max}} = 0.49a_0$ (left column in Fig. 5) is close to the Wigner Seitz radius, the second, $b^2_{\mathrm{max}} = 0.8a_0$ (right column in Fig. 5) is close to the first neighbour distance and allows for assisted focusing by atomic rings in linear collision sequences and is appropriate in cascades calculations, as will be shown in the next section. A first glance to Fig. 5 is sufficient to notice that playing around with these parameters results in fairly different penetration profiles. For clarity, in the following description, we distinguish between the three single crystal cases from the others and we start with the former. This figure also shows the effect of channelling as well as the effect of the two simultaneous collision parameters b_{max} and ξ_{lim} (see Section 2.1.2) on the penetration. At normal incidence, the largest fraction of the beam is channelled and the penetration distribution is dominated by a

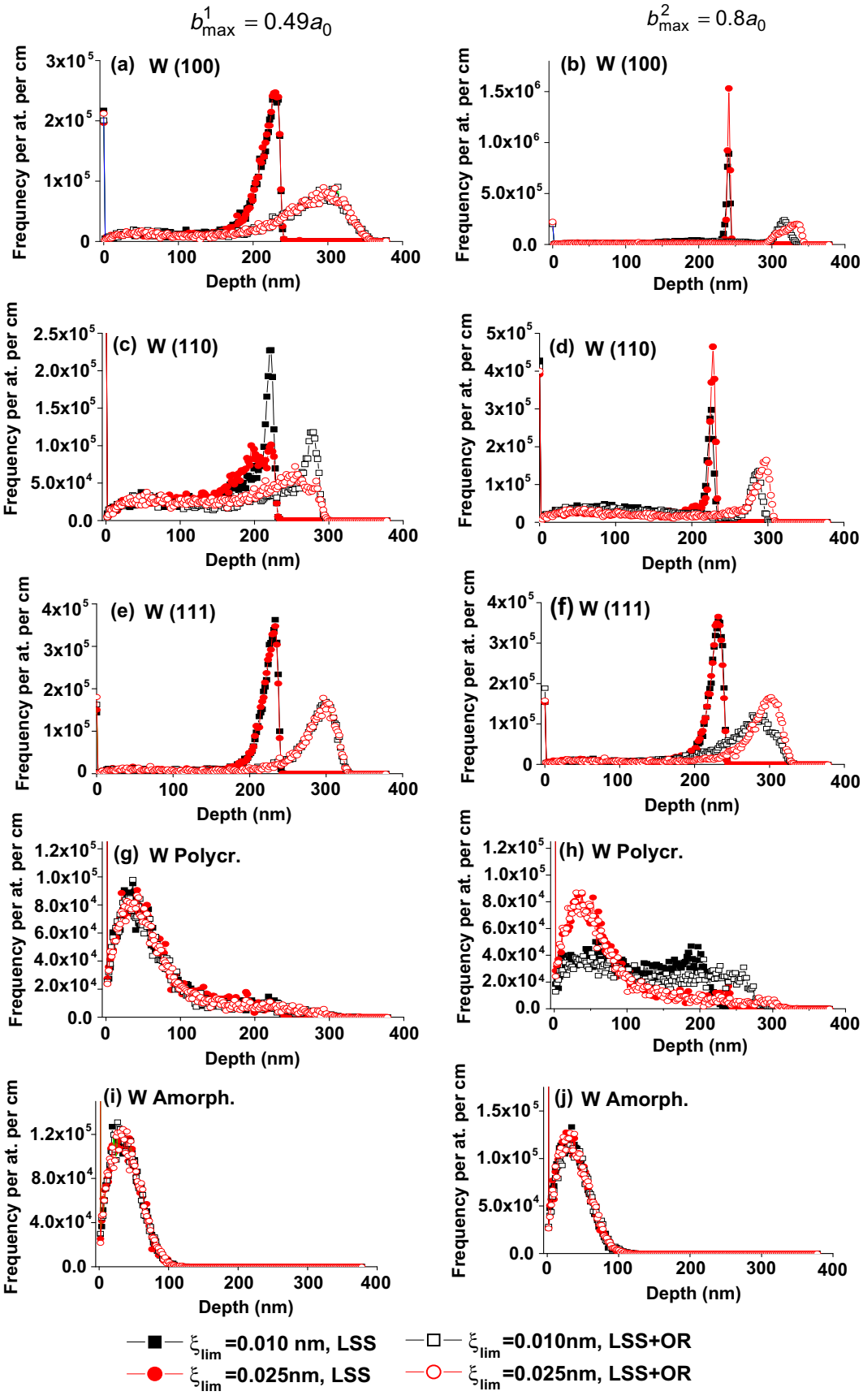

Fig. 5. Depth distribution of He atoms, slowing down with 10 keV kinetic energy on crystalline tungsten with (1 0 0), (1 1 0), (1 1 1) surfaces and on polycrystalline and amorphous tungsten. The effects of two models for inelastic losses are compared. "LSS" corresponds to the standard LSS theory. "LSS + OR" correspond to equipartition between non-local losses according to Lindhard and local losses according to Oen and Robinson.

single mode. The position and the width of this mode strongly depend on the inelastic loss model applied, although the OR losses are normalised to the same stopping power as LSS. The modal penetration is the largest in case of equipartition, illustrating the effect of local losses on the trajectories as computed in the quasi-elastic approximation, with the consequence of more efficient focusing and thus of flux peaking in the centre of the channels. Increasing the maximum impact parameter and thus increasing the number of scattering centres encountered along the trajectory has the effect of increasing the focusing of the trajectories. The consequence is a reduction of the energy loss straggling in the equipartition case, which is particularly significant in the case of {1 0 0} and {1 1 0} surfaces. In this latter case, the modal energy loss is slightly reduced, resulting in slightly larger penetrations.

The rather poor focusing when using b^1_{max} in the case of {1 1 0} surfaces is largely enhanced when using b^2_{max}. This may be explained by the fact that the centres of the channels are bound by rings of four atoms, of which two are at a distance of $0.5a_0$ and two at a distance of $\frac{a_0}{\sqrt{2}}$. Consequently, atoms close to the channel centre are scattered at most by pairs of atoms when using b^1_{max} while they are scattered by rings of four atoms with b^2_{max}, thereby making focusing more efficient. The value $\xi_{lim} = 0.025$ nm is used as standard over most atom-target combinations. The comparison presented here evidences that the effect of ξ_{lim} on the energy loss is minor in comparison to the choice of the inelastic loss model and of the maximum impact parameter.

The tails of the distributions towards low penetration are due to the non-focused or de-focused trajectories and are not significantly influenced by the inelastic loss model. The non-channelled fraction qualitatively scales with the density of the surface scattering centres that are, in decreasing order, {1 1 0}:$\sqrt{2}$, {1 0 0}:1, {1 1 1}:$\frac{1}{\sqrt{6}}$ per a_0^2. The He backscattering yields follow the same scaling: 8% on {1 1 0}, 4% on {1 0 0} and 3% on {1 1 1}. It is not significantly sensitive to the inelastic loss model and to the maximum impact parameter.

We now consider the amorphous and the polycrystalline cases. When an amorphous target model is used, no significant influence of the inelastic model and b_{max} on the depth distribution can be detected. In other words, no focusing effects by distant targets (distance larger than b^1_{max}) is observed and, as expected, the inelastic losses are entirely determined by the stopping cross section, irrespectively to the locality of the electron excitation mechanism.

In the polycrystal case (Fig. 5g and h), a significant tail toward large penetration is observed, associated with channelling.

At energies higher than 10 keV, electronic stopping cross sections of H and He start to differ (Fig. 2) and this influences penetration ranges. However, the relationship between stopping cross sections and ranges in presence of spatial correlations is not obvious, in particular, in the case of channelling. H and He penetration ranges are compared in Fig. 6. In this case the slowing down energy is 60 keV, which corresponds to a difference in electronic stopping cross sections of about 25%. In this case the values $\xi_{max} = 0.01$ nm and $b_{max} = 0.8a_0$ are used. Remarkably, this difference does not affect significantly the range of channelled particles. Differences are observed in a polycrystalline W target, consistent with the offset of stopping cross sections. In this case, the contribution of channelling on penetration ranges is still substantial, resulting in a tail toward large penetrations and a cut-off at the maximal channelling penetration range, with the same efficiency for H and He.

3.2. Permanent displacements

3.2.1. Matching the BCA to experiment

The elastic transfers in most collisions between H or He and W are not sufficient to promote stable Frenkel Pairs (FP). Rather than

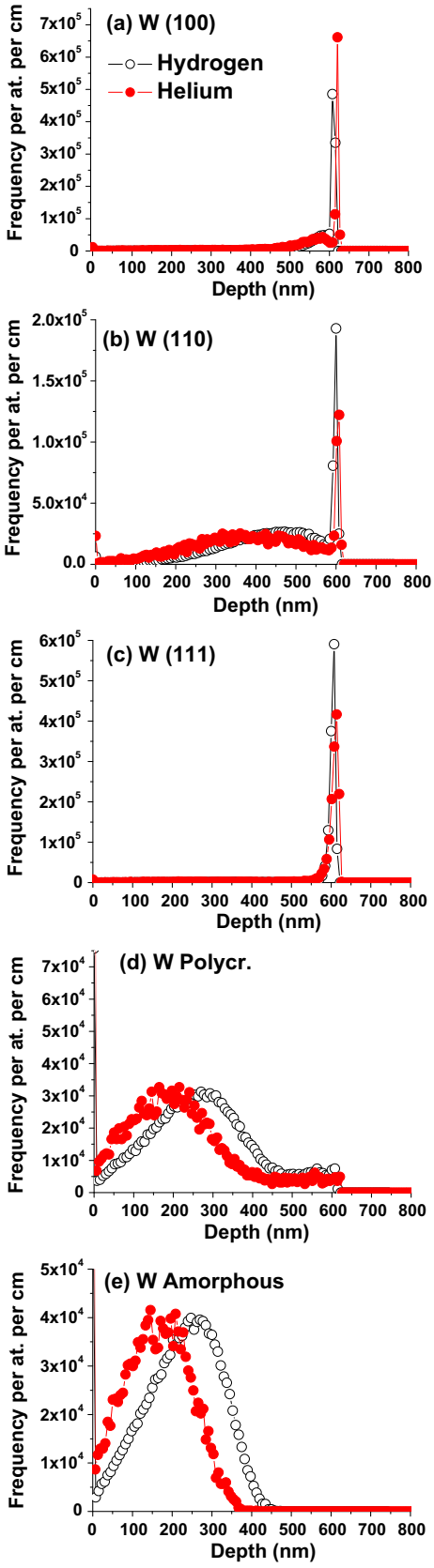

Fig. 6. Depth distributions of He and H atoms with 60 keV slowing down energy on crystalline tungsten with (1 0 0), (1 1 0), (1 1 1) surfaces and on polycrystalline and amorphous tungsten. Inelastic energy losses are computed with the semi-empirical formulas in [18] for H and according to LSS for He (which is found in good agreement with [18] at this energy.

using an energy displacement threshold as in Kinchin–Pease like models, we prefer to account for the physical ballistic displacement mechanisms as much as possible, and thus to acknowledge the essential role of replacement collision sequences. In the BCA, as already mentioned, these are generally short. In full Molecular Dynamics, previous studies in iron demonstrated that their length critically depend on the model potential used [32,33], in particular, in the range of distances where splines are generally used between the equilibrium potential component and a screened Coulomb potential. This problem was discussed in detail elsewhere [33]. It should however be added to the discussion in [33] that, in bcc materials, two successive replacement collisions are sufficient to create a vacancy–interstitial pair with a separation distance larger then $1.7a_0$. If the spontaneous a thermal recombination distance is shorter, then, the separation distance is no important parameter in the efficiency of stable FP production by replacement sequences. What then matters is the frequency of replacement events which—as may be verified from the recoil density [34] and according to the Kinchin–Pease replacement model—only depends on the recoil energy spectrum in the ballistic regime. Since this one is not much dependent on the potential (and being close to follow an E^{-2} dependence on the recoil energy E), it may be expected that the frequency of FP production via replacement sequences will not be much dependent on the potential either.

In tungsten, the recombination distance turns out to be shorter than $1.7a_0$, as we now shall show. For this purpose, we make use of the vacancy distributions observed in tungsten with atomic resolution with a Field Ion Microscopy method (FIM) by the group of Seidman [12,13]. In this experiment, tungsten needles were irradiated with various kinds of heavy ions with energies from 10 to 70 keV and the resulting vacancies were mapped using the same field evaporation technique as presently available in modern atom probes. The number of vacancies observed per "depleted zone" (DZ) are collected in Fig. 7. The straight line is a linear regression which corresponds to a NRT prediction [35] with a displacement energy threshold $E_d = 62.5$ eV. The Molecular Dynamics results are in acceptable agreement with experiment, regarding the fact that initial conditions are different.

We use these results in order to determine a recombination distance in BCA cascades. Similar to what we did in our previous work [10,36] about cascades in other materials (Cu, Au, Cu_3Au, Fe), these are modelled using a displacement threshold equal or lower than the cohesive energy (8.9 eV in tungsten), a binding energy of the atoms to their lattice sites of the same value and a binding energy in replacement events 10 times lower. There is no energy loss in a head on, elastic and isolated replacement collision; however, a replacement event generally involves the simultaneous interaction between three atoms in the row as well as with the rings of atoms surrounding the atomic row along which the sequence propagates. We assume that a small binding energy along the sequence reasonably accounts for their dynamic nature, as was shown in the case of iron [10], copper, gold and, to some extent, ordered Cu_3Au [36]. In order to catch the focusing of $\langle 1\,0\,0\rangle$ replacement sequences by $\{1\,0\,0\}$ rings, $b^2_{max} = 0.8a_0$ was used. $\{1\,1\,0\}$ and $\{1\,1\,1\}$ rings have smaller radii. Using this model and the so-called ZBL potential [18] from Ziegler, Biersack and Littmark, the experiments of Seidman's group were simulated and the number of vacancy–interstitial pairs surviving recombination with a given recombination distance r_c were recorded as a function of r_c. In Seidman's experiment, a single crystal needle was irradiated with a collinear beam. Because of the curvature of the needle, a variety of surface orientations were exposed to the beam. In order to mimic this situation, we model an ion beam normally incident on a polycrystalline flat surface. The results for Kr and for W irradiations are shown in Fig. 8 for eight incident energies between 5 keV and 70 keV. In each of these 16 cases, the r_c value necessary to obtain a matching between the mean number of surviving pairs and the number of vacancies deduced by the NRT fit in Fig. 7 was estimated. The same matching value $r_c = 1.2a_0$ was obtained in all cases, whatever the nature of the incident ions and whatever their energy. For this reason, $r_c = 1.2a_0$ was taken as a recombination distance for the determination of the primary damage, i.e. the amount of stable FP created by He irradiation presented in the next section. Remarkably, fitting on the available MD results by properly modelling internal irradiation leads to the same recombination radius as obtained by fitting to the FIM experiments, modelling the experimental external irradiation.

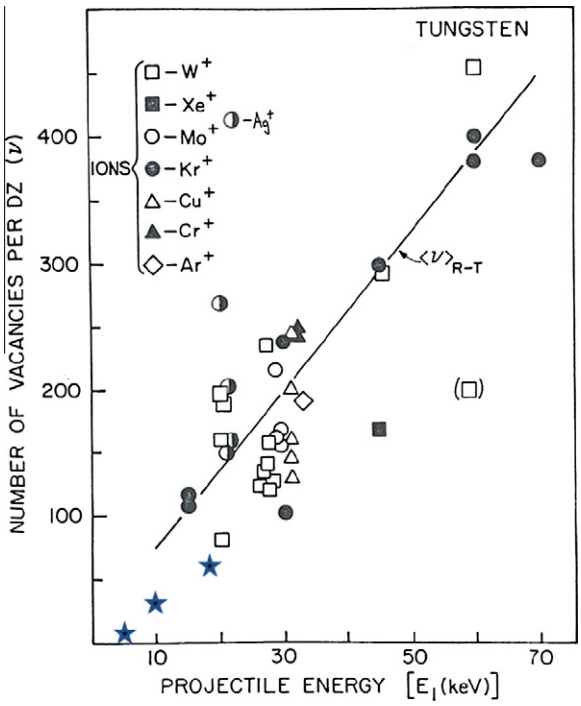

Fig. 7. Number of vacancies observed by Field Ion Microscopy in individual cascades in a tungsten needle irradiated with various heavy ions at various energies [12,13] and at low energy by full Molecular Dynamics [11]. The straight line is a linear regression. The stars indicate the MD results, obtained by initiating primary recoils from lattice sites in an infinite W crystal.

The NRT model (as well as the Kinchin Pease model from which it is originated) makes use of a displacement threshold energy which limits the estimated number of stable Frenkel Pairs. The physical characterisation of this threshold poses a problem as it is found to depend strongly on the recoil direction and the occurrence of replacement sequences.

In the present BCA model, the lowest energy at which a stable FP is produced is the energy needed to produce an interstitial at a distance of $1.2a_0$ from the site at which a recoil is knocked off. It thus requires no more than one replacement in <1 0 0> and <1 1 1> directions and even none in <1 1 0> directions. Since the binding energy in a replacement collision is assumed to be 0.89 eV (10% of that in a non-replacement collision), a He or H incident energy of 10 eV or 40 eV respectively is sufficient in head on collisions. The cross section for such events is however easily anticipated to be quite small. Moreover, they only could occur in the close vicinity of the surface where the induced point defects would anneal.

Disregarding such surface effects, Fig. 9 represents the dependence of the estimated number of FPs separated by more than $1.2a_0$ as a function of the He and H incident energies. The polycrystal model is used and results are also given in case of He slowing down on an amorphous W target. This figure provides no evidence for the occurrence of a displacement threshold energy in the sense

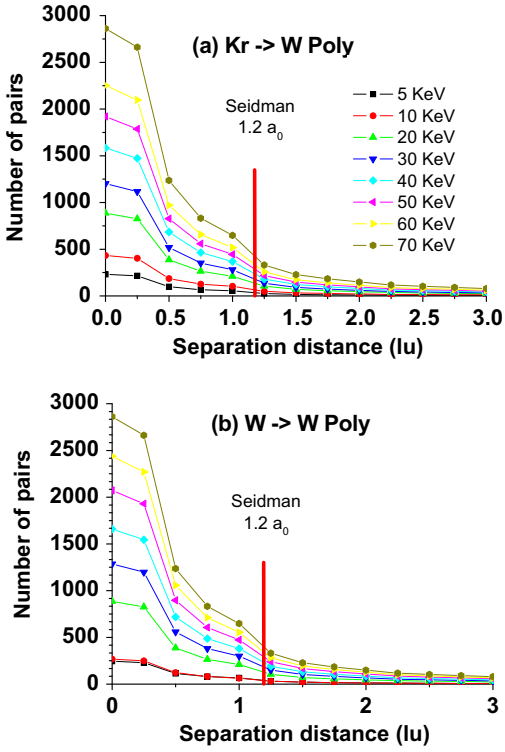

Fig. 8. Mean number of vacancy–interstitial pairs separated by a distance larger than the recombination distance represented in abscissa. The results are shown for various projectile energies incident on a polycrystalline tungsten target in case of irradiation (a) with Kr atoms and (b) with W atoms. The vertical line shows the separation distance for which the simulation results match the experimental values.

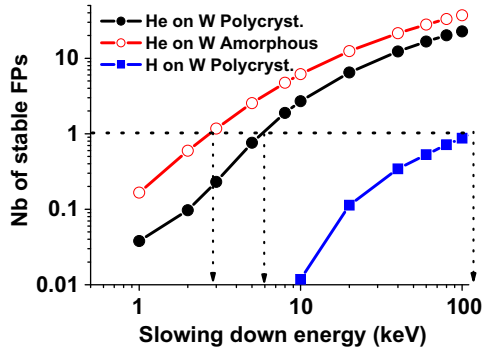

Fig. 9. Dependence of the number of Frenkel Pairs separated by a distance larger than $1.2a_0$ as a function of the He and H slowing down energies. The dotted lines denote the energy needed to produce, in the average, one stable FP per slowing down atom.

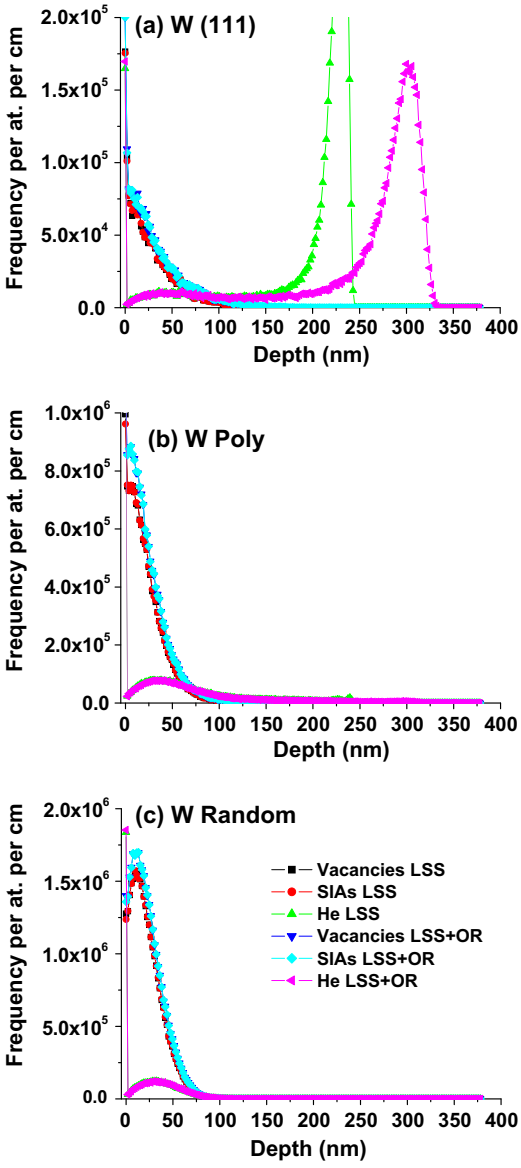

Fig. 10. Depth distribution of primary vacancies and SIAs resulting from He slowing down with 10 keV kinetic energy on crystalline tungsten with (1 1 1) surfaces and on polycrystalline and amorphous tungsten. Then distributions obtained with (1 0 0) and (1 1 0) surfaces (not shown) display similar features as in the (1 1 1) surface case. The effect of the LSS and LSS + OR (see title of Fig. 5) inelastic losses are compared. $b_{max} = 0.8a_0$. Point defect profiles are almost undistinguishable.

of the NRT model. It is however possible to identify some incidence energy characteristics of the dependencies observed. For instance, the dotted lines in Fig. 9 mark the incident energy needed to produce, on average, one stable FP per incident atom. It is 2 and 6 keV in the cases of He on polycrystalline and amorphous W, respectively and above 100 keV for H slowing down on polycrystalline W. Hence, in practical conditions, damage induced by hydrogen will be negligible with regard to that induced by helium.

3.2.2. Frenkel pair distributions under He irradiation

FP depth distributions in the case of 10 keV He implantation are shown in Fig. 10, which are typical of the 5–100 keV range investigated. For the sake of comparison, the He range distributions displayed in Fig. 5 are reproduced. Fig. 10 indicates that the FP distributions are not quite sensitive to the inelastic energy loss model employed and are characterised by a pronounced single mode in the close vicinity of the surface. However, under channelling conditions, their modal frequency is more than one order of magnitude lower than in the case of an amorphous W target. As compared to the same case, subsequently to channelling, the modal FP density in a polycrystal is reduced by a factor of two.

He depth profiles are completely different from the FP profiles. In all cases, the density of implanted He at the surface is up to one order of magnitude smaller than that of FPs. It can however become higher at a distance of 100 nm, depending on the W orientation and model. In particular, in channelling conditions, the majority of the He is implanted in a shallow layer at a depth where no sizeable permanent damage is produced. This is a very

significant result as point defects interact strongly with He or H atoms, forming sessile clusters whereas small pure He clusters are mobile [1]. So, depending on the conditions under which the implantation profile is established, different microstructure evolution patterns are to be expected.

4. Crystal effect in thermal annealing

Using the parameters presented in [1], we simulated one of the He desorption experiment published by Soltan and coworkers [37]. The OKMC simulations, as the experiments, consist of two parts, the implantation sequence followed by the isochronal annealing. Experimentally, 12 appm of 3 keV He along with the amount of FP created by these He atoms were implanted at 5 K in thin films of W with a thickness of 320 nm. In the simulations, a W box of dimension $399 \times 400 \times 1001$ lattice units was used. Periodic boundary conditions (PBC) were applied in two of the three directions. The surface orientation of the single crystal simulated is always perpendicular to the $\langle 0\,0\,1 \rangle$ direction. An isochronal annealing of the whole box was then simulated by increasing the temperature by steps of 2 K every 60 s. As the simulated volume was very small compared to the experimental sample, five simulations were done for each case, changing the seed of the random number generator. Four sets of implantations were done. In one case, the implantation was simulated by introducing cascade debris obtained with the Marlowe code parameterised as described above and taking into account the polycrystalline nature of W. These simulations will be referred to as "M-Poly". In the second set, the He atoms were implanted in W considered to be amorphous. These simulations will be referred to as "M-Amorph" (the difference between the polycrystaline and the amorphous models in Marlowe is given in Section 2). In the third and fourth cases, the He atoms and the associated damage computed with Marlowe were randomly and uniformly redistributed over the whole OKMC simulation box. These simulations will be referred to as "R-Poly" and "R-Amorph" respectively. The experimental implantation rate was 10^{15} s^{-1} m^{-2} which corresponds to the introduction of 16 He per second in the simulation box. For the two first sets of simulations, we thus introduced 16 Marlowe cascades per second in the box. The backscattering yields on the other hand were found equal to 0.38 and 0.49 from the polycrystalline and the amorphous W respectively, so that the amount of implanted He in both cases are comparable but the amount of FPs per implanted He is respectively a third and up to twice the amount per slowing down He. Table 1 provides the numbers of induced point defects per helium atom in the W matrix as they come out of the Marlowe simulations and at the end of the OKMC simulation of the implantation phase at $T = 5$ K, just before the isochronal annealing is started.

In our model, the SIAs and the isolated He atoms are already mobile at 5 K [1] and during the implantation sequence, these defects move. Some reach the surface, some SIAs recombine with neighbour vacancies and some He atoms reach a SIA or a vacancy to form a mixed immobile cluster. As a result, the total number of entities available for the isochronal annealing simulations differ from one simulation to another.

Table 1
Comparison of the numbers of FP per implanted He as given by Marlowe and as remaining at t_0, at the end of an implantation of 12 appm He at a rate of 10^{15} s^{-1} m^{-2}.

	FP Marlowe	Vacancies t_0	SIAs t_0
M-Poly	0.29	0.15	0.08
M-Amorph	2.17	0.85	0.78
R-Poly	0.29	0.17	0.16
R-Amorph	2.17	0.95	0.94

The first significant difference between the M-Poly and the M-Amorph is the amount of recombination taking place during the implantation sequence, as seen in Table 1. With M-Poly, a significant fraction of SIAs also anneal at the surface. This effect continues at the beginning of the isochronal annealing sequence as can be seen in Fig. 11 which represents the evolution of the normalised fraction of defects versus temperature and in Fig. 12 which indicates the net contributions of each defect type (He atoms, SIAs and vacancies).

The results of Fig. 11 clearly evidence the relevance of taking into account the crystal structure of W to reproduce the experimental trends.

One very interesting point is that the behaviour of the "R-Amorph" and the "M-Amorph" as well as "M-Poly" and "R-Poly" simulations are very similar at the lowest temperatures. This can be explained by the fact that the amount of recombinations during the implantation phase is similar.

The main difference between the polycrystalline and the amorphous cases is the amount of induced point defects, as it comes out Fig. 12. This has the consequence that, when the He atoms start moving, the amount of traps they can encounter while travelling

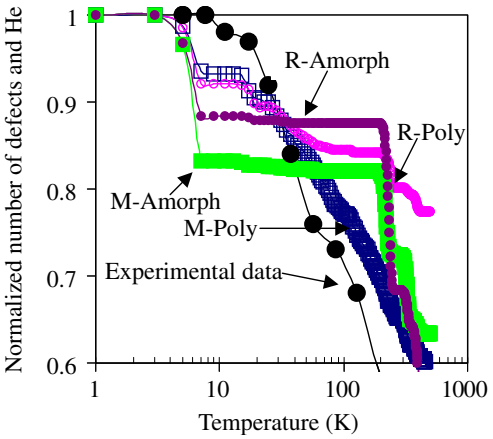

Fig. 11. OKMC simulation of above threshold He desorption experiment. 12 ppm of 3 keV He and the vacancies and SIAs created during the process were introduced in the $399 \times 401 \times 1001$ (in lattice units) simulation box according to the distribution profiles determined using Marlowe considering that W was either a crystal or amorphous or completely at random. The rate of introduction was 10^{15} s^{-1} m^{-2}. C atoms (100 ppm) were introduced as traps for SIAs and vacancies as well as their clusters. The experimental results have been obtained by [36].

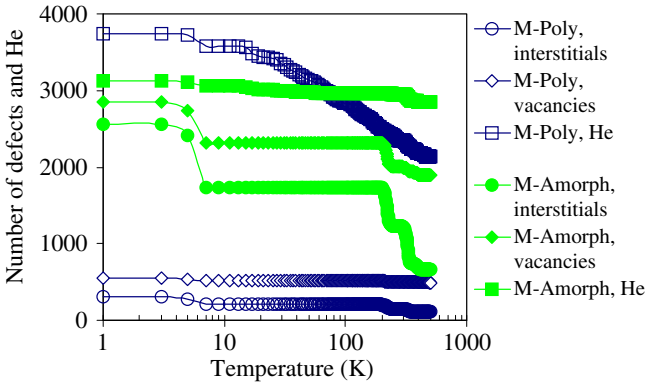

Fig. 12. The three contributions to the "desorption curves", i.e.: the amount of SIAs, vacancies and He atoms as a function of temperature during the isochronal annealing. Results obtained with the "M-Poly" and "M-Amoprh" models are compared.

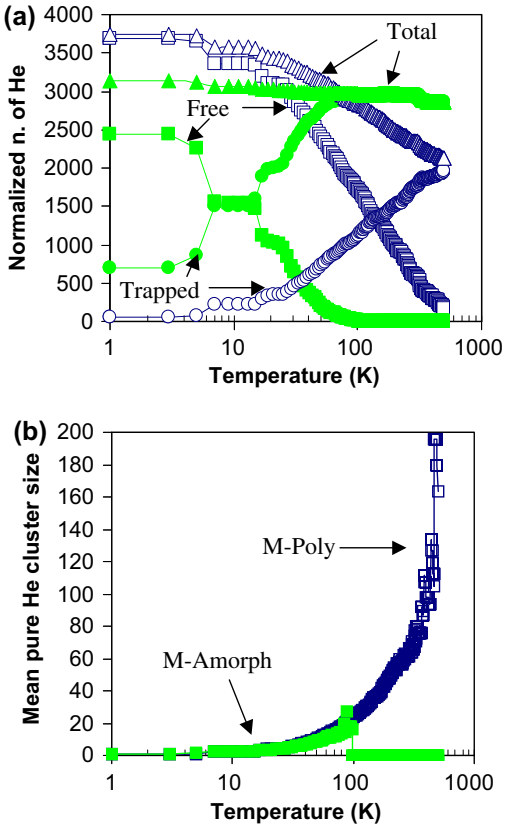

Fig. 13. Comparison of the isochronal annealing of Marlowe cascades implanted in crystal (empty symbols) and in amorphous (filled symbols) tungsten. (a) Shows the total amount of He objects and the two contributions to this amount, i.e. the free He objects, and He trapped in mixed objects. (b) Represents the mean size of the pure He clusters.

towards the surface is much larger in the case of the "amorphous W".

Fig. 13 represents for both cases, the amount of pure He clusters compared to the amount of He in mixed clusters. In our model, the former are mobile while the latter are not [1]. The trapping of the He atoms is thus more significant for the amorphous case as can be seen in Fig. 13. At 10 K, 50% of the He atoms are trapped in the "M-amorph" whereas the same amount of trapping is observed only at 200 K for the "M-Poly" case. At 100 K, all the He atoms are trapped in the "M-Amorph" case and we thus observe a plateau in the evolution of the total number of defects up to higher temperature, whereas for the "M-Poly", pure He clusters are still available, which move and reach the surface. The total number of defects is found to decrease logarithmically. This logarithmic decrease is correlated with the evolution of the migration energy versus He cluster size model which is represented in Fig. 14. Hence, the migration

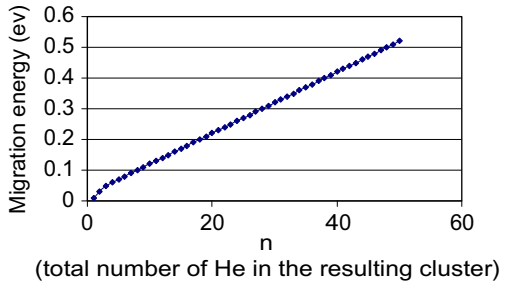

Fig. 14. Mobility law for small He clusters.

of different He cluster types gets activated as the temperature increases, from the smallest to the largest, respectively.

The He clustering which can be characterised by the ratio of the number of isolated He per the number of He in pure He clusters is similar for both cases as the initial He distributions are similar. But clustering is stopped above 100 K for "M-Amorph" because all the He are trapped in mixed clusters.

It is only at 200 K that detrapping becomes possible. The step at this temperature in Figs. 11 and 12 corresponds to the SIA release from carbon traps (0.62 eV binding energy as can be seen in Table 4 of [1]). The next step, at 300 K, corresponds to the dissociation of SIA-He complexes (0.95 eV binding energy).

5. Conclusion

In this paper, we emphasise the importance of allowing for the crystalline structure of polycrystalline tungsten in the estimation of H and He ion ranges as well as in the primary damage induced by the irradiation.

Based on Lindhard's low energy channelling criterion, it is first shown that the channelling probability in polycrystalline tungsten in sizeable up to the 100 keV slowing down energy considered in this work.

The Marlowe code is used to model ballistic atomic trajectories. It is shown that the fraction of the slowing down energy available for producing atomic recoils from nuclear encounters, together with the backscattering energy, is no more than about 10%. The largest part is thus dissipated by electronic excitations and the Marlowe package was extended to account for realistic inelastic loss cross sections beyond the Lindhard regime. It was shown that, at equivalent stopping power, He penetration in the 10–100 keV range is quite sensitive to the character of the inelastic losses (local and non-local), in particular, in channelling conditions. In this case, trajectory fluctuations induced by the quasi-elastic local energy losses allow a more efficient focusing of trajectories into the channels and accordingly larger penetration. Although stopping cross sections differ significantly at 60 keV, H and He atoms slowing down under channelling conditions have similar ranges.

In order to model Frenkel Pairs productions realistically, a simple recombination model, already used for damage calculations in Fe, was parameterized on the basis of point defect observations in irradiated tungsten with atomic resolution. Using this model, it is found that the number of FPs produced is a smooth function of the slowing down energy, whether the tungsten polycrystalline structure is accounted for or not. Simulations indicate that the mean number of FPs produced is significantly reduced in a polycrystal as compared to amorphous tungsten.

Even under channelling conditions, primary damage range profiles are not significantly sensitive to the enhanced channelled He ranges, producing no significant damage. Furthermore, the reduction of damage in polycrystals is found larger than a factor two at all slowing down energies, even when the channelling probability is low. It thus results mainly from spatial correlations in secondary recoil collisions, ordered in short linear focused (replacement) sequences. The consequence of this reduced primary defects production efficiency in the long term are examined by OKMC simulations of thermal annealing experiments following 3 keV implantation at 5 K. The parameterisation of the OKMC model is extensively discussed in a companion paper to this one [1]. It is shown that induced defects act as traps for the otherwise very mobile He at low temperature, inhibiting He desorption. Comparison with experiment suggests that such trapping does not happen in polycrystalline tungsten where the desorption spectral profile is mainly the consequence of He cluster growth in the matrix. Higher energy

implantation should thus produce a higher enough concentration of point defects to cause efficient trapping.

In the 100 keV energy range, penetration depths in the range of 10^3 nm are involved. The depth of the OKMC simulation box used in this study is above 300 nm and takes about 1 day on a recent computer. OKMC simulations one order of magnitude longer are fairly realistic, and the way is thus open to tackling the more general plasma–wall interaction conditions met in fusion technology.

Acknowledgements

The authors wish to thank P. Jung for his comments. This work is supported in part by CEA under the collaborative Contract Number V 3542.001 on Fusion engineering issues, as well as CNRS under the programme interdisciplinaire énergie CHETEX. This research has been done using the CRI supercomputer of the Université Lille1 – Sciences et Technologies supported by the Fonds Européens de Développement Régional.

References

[1] C.S. Becquart, C. Domain, U. Sarkar, A. De Backer, M. Hou, J. Nucl. Mater., this issue.
[2] S. Jumel et al., J. Test. Eval. 30 (2002) 37.
[3] https://fp6perfect.net/site/index.htm.
[4] ftp://ftp.cordis.europa.eu/pub/fp5-euratom/docs/sirena-final-report_en.pdf.
[5] http://cordis.europa.eu/fetch?CALLER=FP7_PROJ_EN&ACTION=D&DOC=22&CAT= PROJ&QUERY=012230a5ad2f:6f70:5a9d5217&RCN=89385.
[6] http://nuklear-server.ka.fzk.de/getmat/.
[7] http://www.efda.org/eu_fusion_programme/scientific_and_technical_publications.htm.
[8] M.T. Robinson, Phys. Rev. B 40 (1989) 10717.
[9] J. Lindhard, Mat. Fys. Medd. Dan. Vid. Selk. 34 (1965) 1.
[10] A. Souidi, M. Hou, C.S. Becquart, C. Domain, J. Nucl. Mater. 295 (2001) 179.
[11] C. Björkas, K. Nordlund, S. Dudarev, Nucl. Instr. Methods B 267 (2009) 3204.
[12] D. Pramanik, D.N. Seidman, J. Appl. Phys. 54 (1983) 6352.
[13] D.N. Seidman, R.S. Averback, R. Benedek, Phys. Status Solidi (b) 144 (1987) 85.
[14] E.V. Kornelsen, A. van Gorkum, Nucl. Instr. Methods 170 (1980) 161.
[15] A. van Veen, L.M. Caspers, Harwell symp, in: S.F. Pugh (Ed.), Inert Gases in Metals and Ionic Solids, AERE report 9733, 1979, p. 517.
[16] J. Lindhard, M. Scharff, H.E. Schiøtt, Mat. Fys. Medd. Dan. Vid. Selk. 33 (14) (1963) 1.
[17] M.T. Robinson, I. Torrens, Phys. Rev. 9 (1974) 5008.
[18] J.F. Ziegler, J.P. Biersack, U. Littmark, Stopping Powers and Ranges of Ions in Matter, Pergamon, New York, 1985.
[19] M. Blackman, Handbuch der Physik, Part 1, vol. VII, Springer-Verlag, Berlin, 1955. p. 377.
[20] J. Lindhard, V. Nielsen, M. Scharff, P.V. Thomsen, Mat. Fys. Medd. Dan. Vid. Selk. 33 (10) (1963) 1.
[21] K.B. Winterbon, P. Sigmund, J.B. Sanders, Mat. Fys. Medd. Dan. Vid. Selk. 37 (14) (1970) 1.
[22] P. Sigmund, Phys. Rev. 184 (1969) 383.
[23] www.srim.org.
[24] J.P. Biersack, J.F. Ziegler, Nucl. Instr. Methods 15 (1982) 93.
[25] M. Hou, M.T. Robinson, Appl. Phys. 17 (1978) 371.
[26] O.S. Oen, M.T. Robinson, Nucl. Instr. Methods 132 (1976) 647.
[27] G. Molière, Z. Naturforsch. 2a (1947) 33.
[28] P. Sigmund, Particle Penetration and Radiation Effects, Springer-Verlag, Berlin, Heidelberg, 2006, ISBN 3-540-31713-9.
[29] W. Brandt, M. Kitagawa, Phys. Rev. B 25 (1982) 5631.
[30] M. Hou, M.T. Robinson, Nucl. Instr. Methods 132 (1976) 641.
[31] K. Gärtner, G. Betz, M. Hautala, G. Hobler, M. Hou, S. Sarite, W. Eckstein, J.J. Jimenez-Rodrigues, A.M.C. Pérex-Martin, E.P. Andribet, V. Konoplev, A. Gras-Marti, M. Posselt, M.H. Shapiro, T.A. Tombrello, H.M. Urbassek, H. Hensel, Y. Yamamura, W. Takeuchi, Nucl. Instr. Methods B 102 (1995) 183.
[32] C.S. Becquart, C. Domain, A. Legris, J.C. van Duysen, J. Nucl. Mater. 280 (2000) 73c.
[33] C.S. Becquart, A. Souidi, M. Hou, Phys. Rev. B66 (2002) 134104.
[34] P. Sigmund, Rev. Roum. Phys. 17 (1972) 823.
[35] M.J. Norgett, M.T. Robinson, I.M. Torrens, Nucl. Eng. Des. 33 (1975) 50.
[36] M. Hou, Nucl. Instr. Methods B187 (2002) 20.
[37] A.S. Soltan, R. Vassen, P. Jung, J. Appl. Phys. 70 (1991) 793.